ESCUELA DE CONSTRUCCIÓN CIVIL
FACULTAD DE INGENIERÍA

Revista de la Construcción
Journal of Construction

Research Article

Ultimate capacity prediction of RC and SFRC beams with low shear span-depth ratio using NLFEA and inverse analysis

Carlos A. Benedetty [1, *], Ingrid R. Irreño [1], Juan J. Martinez [1], Luiz C. Almeida [1], Leandro M. Trautwein [1], Pablo A. Krahl [2]

[1] University of Campinas, School of Civil Engineering, Architecture and Urban Design, R. Saturnino de Brito, Campinas, SP (Brazil), bendedettiV8@gmail.com, ingridpal2393@gmail.com, juandejesusmartinezp@gmail.com, almeida@fec.unicamp.br, leandromt@fec.unicamp.br

[2] Mackenzie Presbyterian University, Department of Civil Engineering Campinas, SP (Brazil), pablo.krahl@mackenzie.br

*Correspondence: bendedettiV8@gmail.com

Received: 15.02.2022; **Accepted:** 17.10.2022; **Published:** 29.12.2022

Citation: Benedetty, C. A., Irreño, I. R., Martinez, J. J., Almeida, L. C., Trautwein, L. M., and Krahl, P. A. (2022). Ultimate capacity prediction of RC and SFRC beams with low shear span-depth ratio using NLFEA and inverse analysis. Revista de la Construcción. Journal of Construction, 21(3), 717-736. https://doi.org/10.7764/RDLC.21.3.717.

Abstract: In this study, the capacity and ultimate behavior of Reinforced Concrete (RC) and Steel Fiber Reinforced Concrete (SFRC) beams are evaluated. Nonlinear Finite Element Analysis (NLFEA) and the inverse analysis technique were used to model its structural response using the ATENA finite element software. The smeared crack approach, the crack band model, and advanced constitutive models were used to reproduce concrete fracture. The analyzed beams were subjected to rupture in a four-point bending test setup. The relationship between the shear span and the depth of the beams was 1.5. Four scenarios were analyzed, RC beams with and without stirrups, and SFRC beams without stirrups with volumes of 0.57% and 0.76%. The results obtained in the modeling are discussed in terms of the ability of the models to numerically reproduce the relationships: load versus displacement, load versus strain, crack patterns, and failure modes. The analysis techniques allowed to reproduce the experimental response of the beams with good agreement. They show great potential to solve structural engineering problems.

Keywords: Beams; steel fibers; shear; inverse analysis; finite elements.

1. Introduction

Steel Fiber Reinforced Concrete (SFRC) is increasingly used in several civil construction applications (Di Prisco & Plizzari, 2004; Serna, Arango, Ribeiro, Núñez, & Garcia-Taengua, 2009; Kasuga, 2017; Cugat et al., 2020). The composite material has many advantages compared to normal concrete regarding the residual strength provided by the fibers. When the cementitious matrix is cracked, debonding and sliding of the fibers are the mains mechanisms for providing residual strength (Li, Xu, Chi, Huang, & Li, 2017; Li et al., 2018; Poveda et al., 2020). The transfer and redistribution of stresses produced during the fracture process provide improvements in mechanical properties such as: tensile strength, energy absorption, ductility and toughness (Barros & Figueiras, 1999; Wang, Wu, & Wang, 2010; Lee, Cho, & Choi, 2017). Mechanical and geometric properties of the steel fibers and their interaction with the matrix have an important role in the structural performance of SFRC elements. Factors associated with properties of fibers, such as tensile strength, anchorage, length, diameter and volume fraction, are some variables that may influence post-cracking behavior (Banthia & Trottier, 1994).

The prediction of ultimate capacity and behavior of reinforced concrete structures is highly studied in structural engineering. Recently, Nonlinear Finite Element Analysis (NLFEA) have been used to analyze a variety of engineering problems. The modeling of structures using NLFEA is widely explored through finite element programs (e.g. ABAQUS, ATENA, DIANA FEA, etc.) (Sanabria Díaz, Sarmiento Nova, Teixeira da Silva, Mouta Trautwein, & de Almeida, 2020; de Souza & Breña, 2020). However, SFRC modeling is limited, since the anisotropy and heterogeneity of the material lead to more complex simulations. Several strategies have been applied to predict the response and phenomena involved in the fracture of SFRC.

Two approaches are known for being used according to the problem modeling scale, namely, modeling through meso-models, where fibers are discretely and randomly represented in the finite element mesh (Zhang, Huang, Yang, Xu, & Chen, 2018; Zhang, Zhang, Liao, Wang, & Zhao, 2020), and modeling through macro-models, in which there is no spatial representation of the fiber. The first approach represents the most realistic problem; nevertheless, a high computational cost is required for the simulation (Sheng, Zhang, & Ji, 2016). In cases where large structures need to be simulated, this feature is disadvantageous and has little potential for practical applications. On the other hand, in the second approach fracture is governed by constitutive laws that reproduce the energy released during the fracture process of the material. Finite element programs like the ones mentioned above use this latter approach. In these, fractures due to tensile are reproduced through softening functions.

The softening functions are of great importance in NLFEA due to describing how energy is dissipated during a fracture. Post-peak tensile stresses are associated with crack openings. For conventional concrete, softening is frequently described by the Hordijk exponential function (Hordijk, 1991). Regarding the SFRC, the function has limitations for describing this behavior. In this instance, specific functions need to be determined through experiments (e.g. Direct tensile test). Several researchers have reported complexities and limitations for carry out direct tensile test (Cattaneo & Rosati, 1999; Dupont & Vandewalle, 2002). As an alternative, three- or four-point bending tests on prismatic specimens are combined with inverse analysis techniques to find the function indirectly. Basically, the technique consists of an iterative procedure in which from of experimental load versus displacement or Crack Mouth Opening Displacement (CMOD) of the notched specimens, wherein the softening function parameters are determined through finite element model calibration.

Despite the large number of studies on SFRC modeling using inverse analysis technique (Uchida, Kurihara, Rokugo, & Koyanagi, 1995; Planas, Guinea, & Elices, 1999; de Oliveira e Sousa & Gettu, 2006; de Montaignac, Massicotte, Charron, & Nour, 2012; Gribniak, Kaklauskas, Hung Kwan, Bacinskas, & Ulbinas, 2012; Woo, Kim, & Han, 2014; Nour, Massicotte, de Montaignac, & Charron, 2015; Yoo, Yoon, & Banthia, 2015; Gali & Subramaniam, 2018; Soltanzadeh, Cunha, & Barros, 2019), many of them are limited to study small-scale elements (specimens) without reinforcement. Also, the strength and ultimate behavior of structural elements of a higher scale combined with analysis techniques have been less explored (Kannam & Sarella, 2018). Additionally, recent NLFEA studies focused on predicting the ultimate capacity and fracture behavior of SFRC beams failing in shear, showed the great difficulty to obtain reliable results (Barros et al., 2021).

In this paper the ultimate behavior of Reinforced Concrete (RC) and SFRC beams with low shear span-to-depth ratio is studied through NLFEA and inverse analysis. The main objectives are to experimentally analyze the failure modes in beams and assessment the ability of techniques for predicting its structural behavior using ATENA program. In this way, the work contributes to increasing the bench of solutions for structural engineering problems supported by the great potential of constitutive models and parameters used in the simulations for the prediction of ultimate capacity, fracture behavior and failure modes.

2. Materials and methods

The experimental program presented in this paper was part of a research that studied the influence of steel fibers on shear failure mechanisms in beams (Benedetty, 2018). Three groups of beams were analyzed in this study: RC beams without stirrups, RC beams with minimum shear reinforcement and SFRC beams without shear reinforcement.

2.1. *Material properties*

Two types of concrete were used in the experimental study, Normal Concrete (NC) and Steel Fiber Reinforced Concrete (SFRC). The two types of concretes used were supplied by a local concrete company (Campinas, São Paulo). The mixtures consisted of Brazilian cement type CPII–Z, coarse basalt aggregate and river sand with maximum sizes of 19 mm and 2.4 mm, respectively. Because the NC beams were cast on different dates, two batches of NC were used. The RC beam with stirrups was cast with batch 1 and the beam without stirrups with batch 2. Regarding the SFRC beam, these were cast with batch 2 and hooked-end steel fibers DRAMIX 3D 45/30BL of 30 mm in length and 0.62 mm in diameter. The fiber contents were 0.57% and 0.76%, Table 1 shows the dimensions and mechanical properties of the fiber.

Table 1. Properties of hooked-end steel fibers.

Length, l_f [mm]	Diameter, d_f [mm]	Aspect ratio, l_f/d_f [-]	Tensile strength, f_u [MPa]	Elastic modulus, E_f [MPa]
30	0.62	45	1270	210000

2.2. *Characterization tests*

2.2.1. Normal concrete and SFRC

All types of concrete were characterized at ages greater than 28 days. The specimens were tested on the same day as the test of the beams. Compressive strength was determined by axial compression tests on six cylindrical specimens of 100 mm in diameter by 200 mm in height, in accordance with the recommendations of the ABNT NBR 5739 standard (ABNT, 2007). The elastic modulus was measured following guidelines from the ABNT NBR 8522 standard (ABNT, 2008), three of the six specimens used in the axial compression tests of each batch were used for its determination. Indirect tensile strength of NC was measured by the Brazilian test on six cylindrical specimens of 100 mm in diameter by 200 mm in height, following the specifications of the ABNT NBR 7222 standard (ABNT, 2011). Table 2 shows the mean values of the mechanical parameters for each type and batch of concrete.

Table 2. Mechanical properties of concretes.

Nomenclature	Batch	f_c [MPa]	f_t [MPa]	E_c [GPa]	G_F [N/m]	Age [days]
NC	1	41.06 (1.85)	3.37 (0.26)	26.08 (1.61)	142.50 (–)	48
	2	38.98 (1.66)	4.18 (0.22)	27.13 (2.27)	184.50 (21.13)	38
SFRC–0.57	–	37.26 (1.84)	4.83 (0.34)	27.18 (0.83)	–	39
SFRC–0.76	–	39.64 (0.81)	4.85 (0.60)	30.19 (1.47)	–	40

[Note] f_c = compressive strength, f_t = tensile strength, E_c = elastic modulus, G_F = fracture energy, and (s.d.) = standard deviation.

An important parameter to simulate fracture processes in quasi-brittle materials is fracture energy (G_F), that is, the energy necessary to completely fracture a unit area of concrete. In this study, it was only measured in the second batch of NC, through three-point bending test in four prismatic specimens of 100 mm × 100 mm × 400 mm and notch of 50 mm in height. Test variables such as the loading rate (0.05 mm/min) and the span between supports (300 mm) were adopted following the JCI-S-001-2003 standard (JCI, 2003). In the absence of the experimental value of the fracture energy of the first batch of NC, this was estimated using the equation recommended by the fib Model Code 2010 (FIB, 2010) (Equation 1).

$$G_F = 73 \cdot (f_{cm})^{0.18} \quad (1)$$

where f_{cm} is the mean compressive strength of the concrete.

In order to capture the post-cracking response of the SFRC, specimens of the same dimension were tested using the same test setup, however, a higher loading rate (0.2 mm/min) was adopted for those samples, as specified in the JCI-S-002-2003 standard (JCI, 2003). In Figure 1 the load versus displacement responses measured for the two volume ratios of SFRC are presented, a post-peak softening behavior could be observed in both cases.

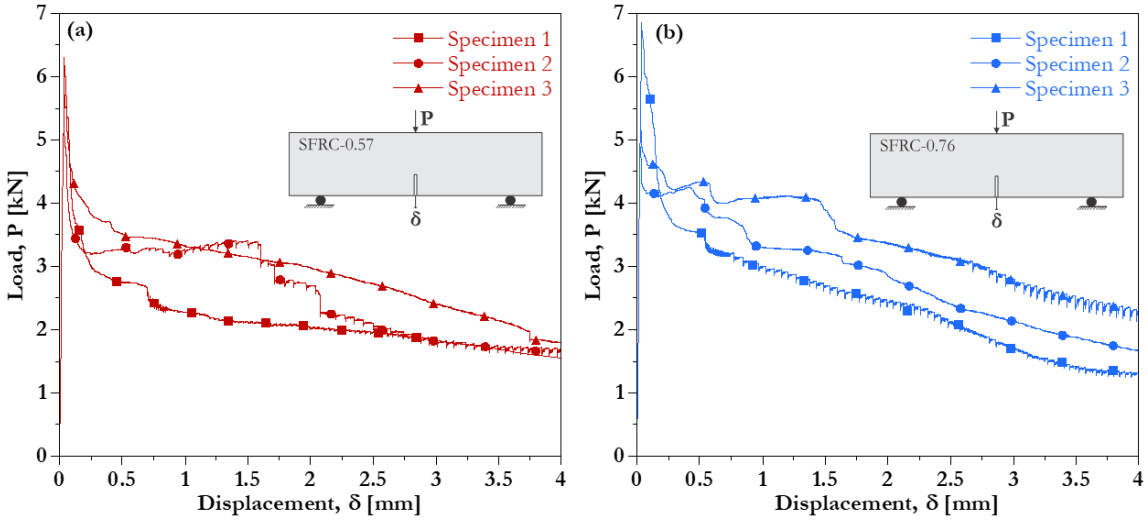

Figure 1. Load versus displacement responses of notched specimens: (a) SFRC–0.57 and (b) SFRC–0.76.

The tensile strength in bending of the SFRC was calculated from the results of the three-point bending test with use of the following equation:

$$f_t = \frac{3PL}{2b(h-a)^2} \tag{2}$$

where P is the cracking load, L is the span between supports, b the specimen width, h specimen depth and a the height of the notch.

2.2.2. Reinforcement steel bars

Three diameters of steel bars were used as reinforcement in the beams. Bars of 5 mm for stirrups, 8 mm for stirrup-holders and 16 mm for longitudinal reinforcement. Two batches of reinforcement steel bars were used for this last diameter. The NC beams were cast with batch 1 and the SFRC beams with batch 2. Direct tensile tests were performed to determine the stress versus strain curve of the bars (Figure 2), and, additionally, mechanical properties such as: yield strength (f_y), yield strain at limit of proportionality ($\varepsilon_{y,LOP}$) and elastic modulus (E_s).

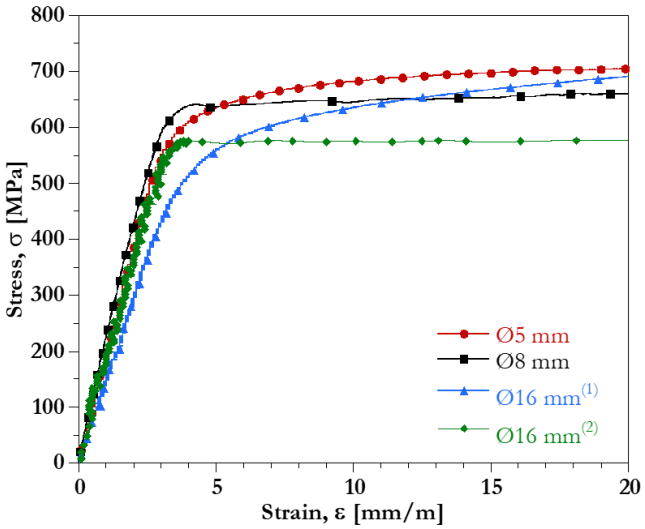

Figure 2. Stress versus strain curves of reinforcement bars.

The tests followed the recommendations of the ASTM E8/E8M-16a (ASTM, 2016) and ASTM 370-17 (ASTM, 2012) standards. Table 3 shows the mechanical properties of the reinforcements.

Table 3. Properties of reinforcement bars.

Diameter [mm]	E_s [MPa]	$\varepsilon_{y,\,LOP}$ [mm/m]	f_y [MPa]	f_u [MPa]
5	193880	2.73	632.09	703.87
8	192126	3.18	642.34	750.93
16 (1)	182720	2.30	581.65	795.07
16 (2)	190450	3.15	557.27	680.20

[Note] E_s = elastic modulus, ε_y = yield strain at limit of proportionality, f_y = yield strength, and f_u = ultimate strength.

2.3. *Test setup and characteristics of beams*

In the present study, the behavior and shear mechanisms of four beams with different failure mechanisms were analyzed and discussed. They all have a rectangular cross section of 150 mm × 400 mm and 2100 mm in length. These were tested in a four-point bending configuration, and the load was applied by a hydraulic actuator to a metal profile, which distributed it in two contact areas on the upper surface of the beam, through the use of steel plates of 100 mm × 150 mm × 20 mm and 37 mm diameter rollers. The support system had the same components; however, the right support lower plate restricted the longitudinal roller displacement in the beam direction, working as a fixed support. The left support allows longitudinal displacement, whose used test setup is shown in Figure 3, in addition to the geometric characteristics and reinforcements details of the beams. The relationship between the shear span (a) and the effective beams depth (d) was 1.5, a constant value in all tests.

In order to simplify the naming of the beams throughout this study, the nomenclatures established according to their characteristics were the following: Beams made of normal concrete (NC), beams made of steel fibers reinforced concrete (SF), beams without stirrups (L) and beams with stirrups (S). To specify the fiber content, we added the numbers 0.57 and 0.76 to the nomenclatures. Thus, NC-S refers to a beam made of normal concrete with stirrups and SF-L-0.76 refers to a steel fiber reinforced concrete beam without stirrups and with a fiber content of 0.76%.

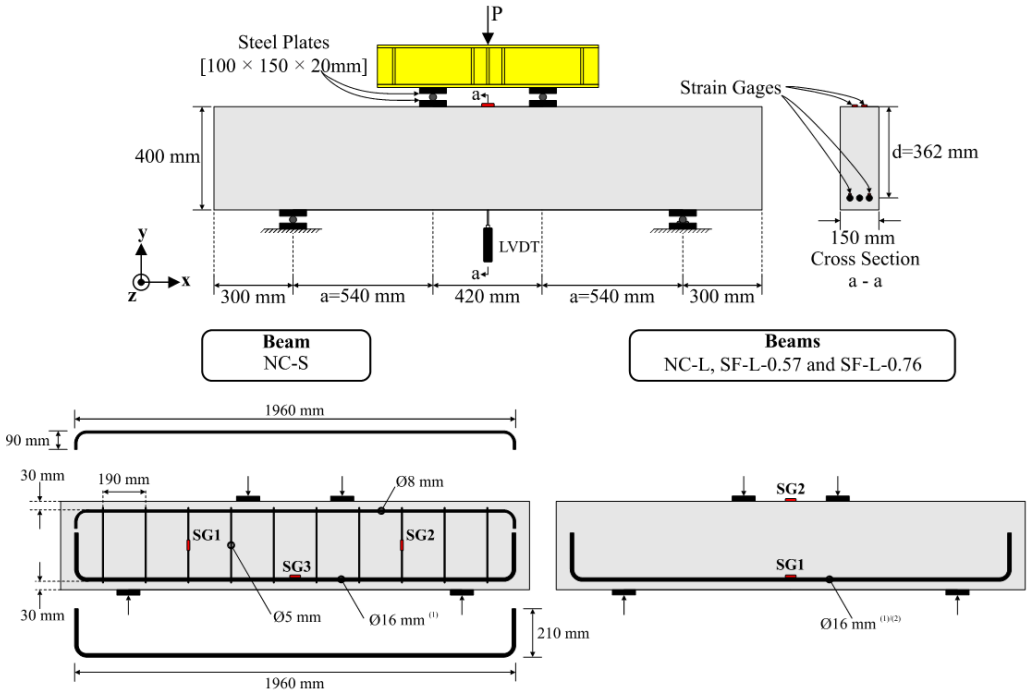

Figure 3. Test setup, instrumentation and reinforcement details.

2.4. *Numerical methodology*

In order to analyze and numerically validate the nonlinear behavior of the beams, simulations using the commercial finite element program ATENA were developed. In this program, the phenomena of fracture and plasticity of concrete can be analyzed with the use of the fracture-plastic constitutive model (Červenka & Papanikolaou, 2008). The crack band theory (Bažant & Oh, 1983) and the smeared crack approach are integrated into the finite element program to reproduce the crack propagation and crack opening phenomena in the analysis of reinforced concrete structures. In the crack band model, the cracking in the fractured process zone is assumed to be smeared along a band. This assumption makes it possible to establish a relationship between the large strains (fracture strains) of cracked concrete and the corresponding crack widths. Equation 3 establishes the relationship between these parameters. In ATENA the crack band width (L_t) is defined as the projected dimension of the finite element measured perpendicular to the orientation of crack.

$$\varepsilon_f = \frac{w}{L_t} \tag{3}$$

where ε_f is the fracture strain, w the crack width, and L_t the crack band width.

The nonlinear behavior of the material can be modeled through material models, which govern the behavior material over functions that reproduce the relationships: stress (σ) – strain (ε), stress (σ) – displacement (δ) or stress (σ) – crack opening (w). Figure 4 shows a scheme of the material models that were used in the simulation of RC and SFRC beams.

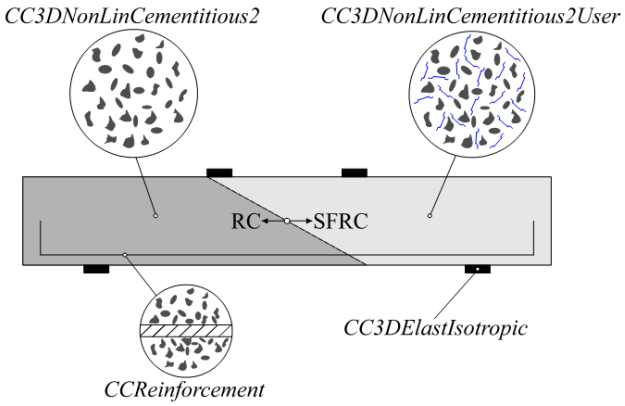

Figure 4. Material models for NLFEA in ATENA.

2.4.1. Material model for normal concrete

The CC3DnonLinCementitious2 model was used to simulate the behavior of normal concrete. In this instance, the dissipated fracture energy due to tensile stress, is governed by the Hordijk softening function (Hordijk, 1991) (Equation 4).

$$\frac{\sigma}{f_t} = \left\{1 + \left(c_1 \frac{w}{w_c}\right)^3\right\} \exp\left(-c_2 \frac{w}{w_c}\right) - \frac{w}{w_c}(1 + {c_1}^3)\exp(-c_2) \tag{4}$$

where σ is normal tensile stress at crack, f_t is the tensile strength of concrete, w is the crack opening and w_c is the crack opening when σ=0. Parameters c_1 and c_2 are coefficients relative to the adjust function with values 3 and 6.93, respectively.

Figure 5(a) shows the softening curve, the area under the exponential curve is the fracture energy (GF), associated with parameter w_c in Equation 5.

$$w_c = 5.14 \frac{G_F}{f_t} \tag{5}$$

The concrete compressive failure is based on the Menetrey & Willam (1995) failure criterion, which depends on basic concrete properties such as axial compressive strength (f_c') and plastic strain (ε_{cp}). For practicality, to describe the pre-peak and post-peak compression regimes ATENA adopts the stress-plastic strain and stress-displacement relationships of Figures 5(a) and 5(b) (Červenka, Jendele & Červenka, 2021). Each function reproduces the hardening in the plastic regime and softening at rupture. The parameters to define the hardening function in the pre-peak regime are: compressive strength (f_c'), plastic strain (ε_{cp}) and compressive stress (f_{c0}), the latter refers to the value of stress when the plasticity phenomenon begins. Figure 5(b) presents the model parameters: compressive strength, tensile strength, and elastic modulus. The curve is calculated according to Equation 6.

$$\sigma = f_{c0} + (f_c' - f_{c0}) \sqrt{1 - \left(\frac{\varepsilon_{cp} - \varepsilon}{\varepsilon}\right)^2} \tag{6}$$

With regard to the softening function in the post-peak regime, concrete behavior is represented linearly through the fictitious compression plane model (Figure 5(c)), which establishes that softening after being cracked depends on a parameter known as post-peak plastic displacement (W_d), validated by experimental studies by van Mier (1986), wherein a value 0.5 mm can be adopted for normal concrete.

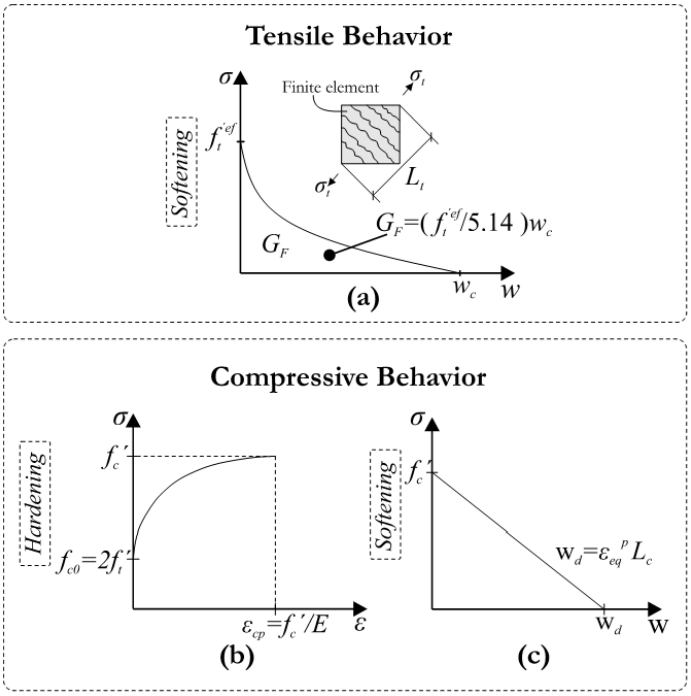

Figure 5. Tensile and compression models: (a) exponential softening in tensile (Hordijk, 1991), (b) hardening in compression (Červenka, Jendele & Červenka, 2021) and (c) linear softening in compression (van Mier 1986).

2.4.2. Material model for steel fiber reinforced concrete

The model *CC3DnonLinCementitiousUser* was used to simulate the SFRC, which allows to define specific user-defined functions that numerically reproduce post-cracking effects during the fracturing process. These functions relate the dimensionless tensile stress (σ_t/f_t) with the material fracture strain (ε_f). The dimensionless stress is a ratio between the acting tensile stress (σ_t) and the maximum tensile strength of SFRC (f_t). The fracture strain (ε_f) corresponds to the residual strains in the post-peak regime. Material characterization tests to measure strains are quite complex, so inverse analysis techniques can be used to indirectly obtain the function parameters. Sajdlová (2016) presents a methodology to simulate SFRC using the *CC3DnonLinCementitiousUser* material model. The tensile response of material can be represented as a function obtained by an iterative process that correlates the experimental load-displacement curve of the three-point bending test in notched specimens with the numerical curves obtained by simulation using ATENA. A scheme of the technique is provided in Figure 6. The basic process of methodology is summarized below.

1. To test several notched specimens of SFRC and plot the P – δ curves, identifying the values of cracking load (P_{crack}) and peak load (P_{max}).
2. To calculate the average value of the flexural tensile strength (f_{tm}), from the cracking load (P_{crack}) or maximum load (P_{max}) in case it is impossible to identify the cracking load on curve, and the dimensions of the ligament surface of the specimens, using Equation 2.
3. To insert an initial softening tensile function (bilinear) in the material model parameters, Figure 6 presents an example of this function. The abscissa of zero dimensionless stress point corresponds to the maximum fracture strain (ε_{fmax}), this can be determined using the crack band model equation (Equation 3), where the crack width (w) is adopted as the approximate value of maximum crack observed on the test (i.e. 6 mm) and the crack band size (L_t) is adopted as the finite element size in the notch of specimen (i.e. 2 mm).
4. To model the specimen in ATENA, defining the finite element mesh, boundary conditions and monitoring points to capture magnitudes of interest, e.g. applied load (P), vertical displacement at mid-span (δ) and crack width on the notch tip (w).

5. To plot the average experimental curve with the numerical curve and calculate the factor (R_i) for several post-peak displacements (δ_i) along the curves. The factor is defined as a ratio between the numerical load (P_{num}) and average experimental load (P_{exp}) for specific displacements (δ_i).
6. To calculate the fracture strains ($\varepsilon_{f,i}$), based on the numerical crack width (w) associated to each displacement (δ_i), using the crack band model (Equation 3). The crack width values used in the calculation correspond to the numerical crack width on the notch tip (obtained in step 4). The fracture strain values found correspond to the abscissa of the new tensile softening function. The ordinates are determined by interpolating dimensionless stresses (σ_t/f_t) of the initial function and multiplying them by the factor R_i.
7. Insert the new function in the material model parameters and repeat steps 4–6 iteratively, until the calibrated numerical curve is found.

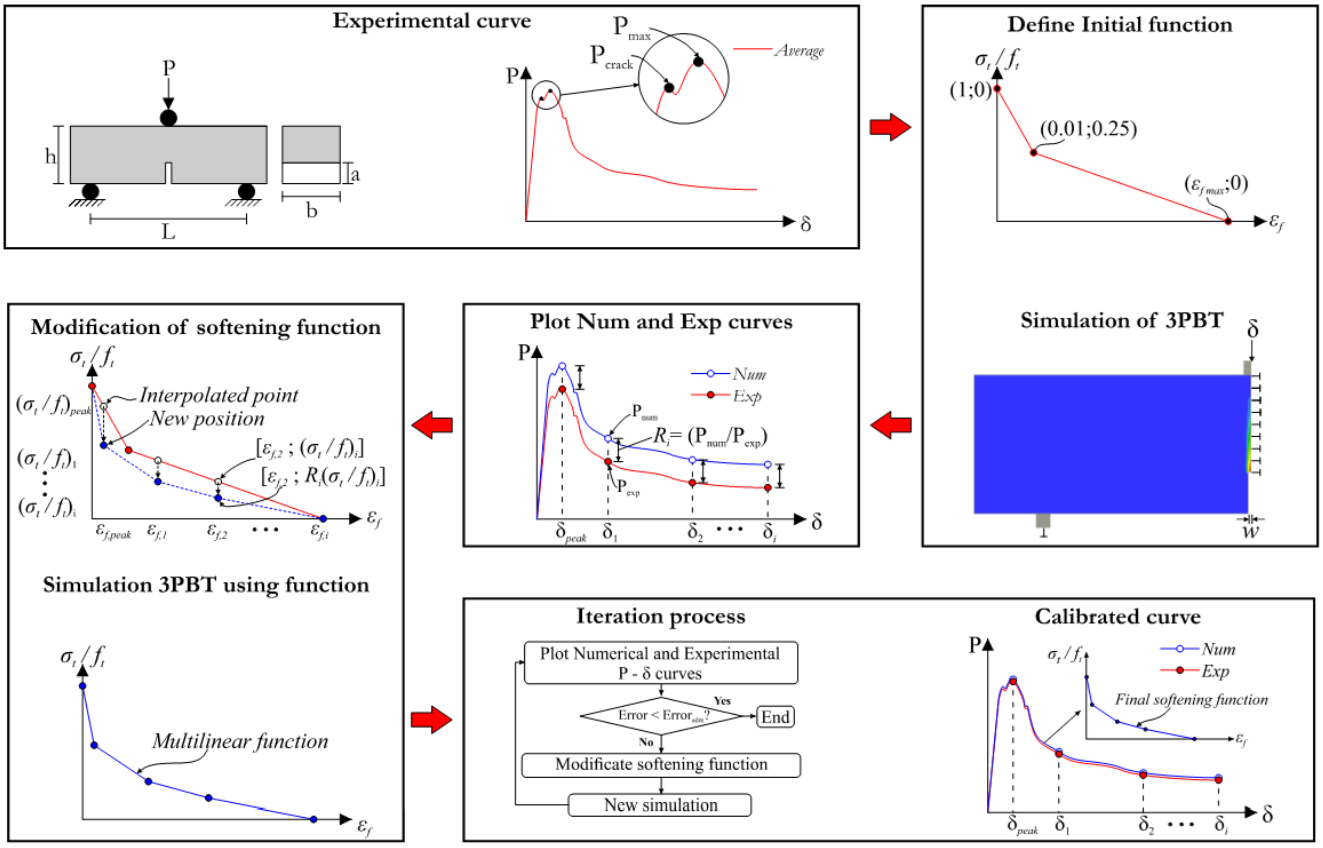

Figure 6. Scheme of the inverse analysis technique.

2.4.3. Material model for reinforcement bars and steel plates

The reinforcing bars were simulated with a *CCReinforcement* model. The hypothesis of perfect bond between concrete and reinforcement was adopted. The stress–strain relationships of the material were reproduced in the simulation using multilinear functions (Figure 7(a)). The points of the function were obtained from the stress–strain curves of Figure 2. The loading plates, were simulated using the *CC3DElastIsotropic* model, in this instance, the relation stress–strain is described by a linear function (Figure 7(b)), where only the steel elastic modulus is necessary to define it.

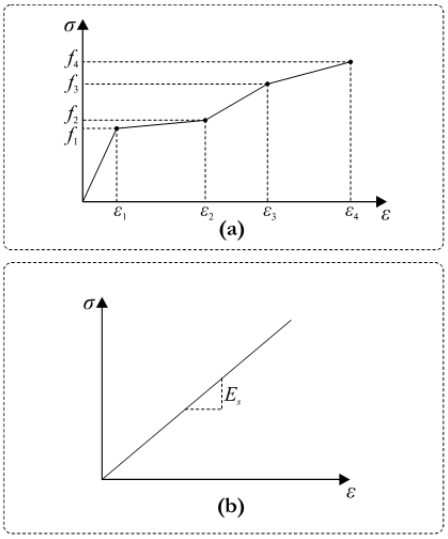

Figure 7. Stress versus strain relationships: (a) reinforcement and (b) loading plates.

2.4.4. Finite element mesh

The finite element mesh of the specimen and the beams were generated with GID v10.0.9 preprocessor (GID, 2009). The mesh geometry and boundary conditions of the models are shown in Figure 8. Due to the symmetry conditions of the problem, in both cases half of the element was simulated. This simplification reduced the processing time of the models. The plane stress state condition was adopted for the notched specimen model (Figure 8(a)). A 4-node shell finite elements *CCIsoQuad4_2D* were used for simulating the notched specimens (prisms). Greater refinement was applied in the notched region (2 mm × 2 mm). 3-node triangular shell finite elements *CCIsoTriangle3_2D* were used to increase the element dimension outside the notched region. The notched specimen model had 1959 quadrilateral elements and 225 triangular elements.

Three-dimensional models were used in the RC and SFRC beams. A 20-node hexahedral finite element *CCIsoBrick20_3D* was used to simulate the concrete and loading plates of beams (Figure 8(b)). Truss element *CCBar_3D* was used for the steel bars embedded in the concrete. The finite element size for the concrete and loading plates were 30 mm × 30 mm × 30 mm and 25 mm × 25 mm × 20 mm, respectively. The models without stirrups consisted of 117 truss elements and 2323 hexahedral elements, and the models with stirrups contained 232 additional truss elements.

2.4.5. Boundary conditions

Boundary conditions in the numerical models are shown in Figure 8. The support plates were constrained in the y-axis allowing displacement in the x-axis and rotation, while the displacements in the symmetry plane of the notched specimen and the beam were constrained in the x-axis allowing displacement in the y-axis. A prescribed displacement was assigned along the central axis of the loading plate. The displacements were 8 mm and 16 mm for the NC and SFRC beams, respectively. The contact between the steel plates and the concrete was simulated using a master-slave condition without the need to join the finite element mesh nodes of both materials.

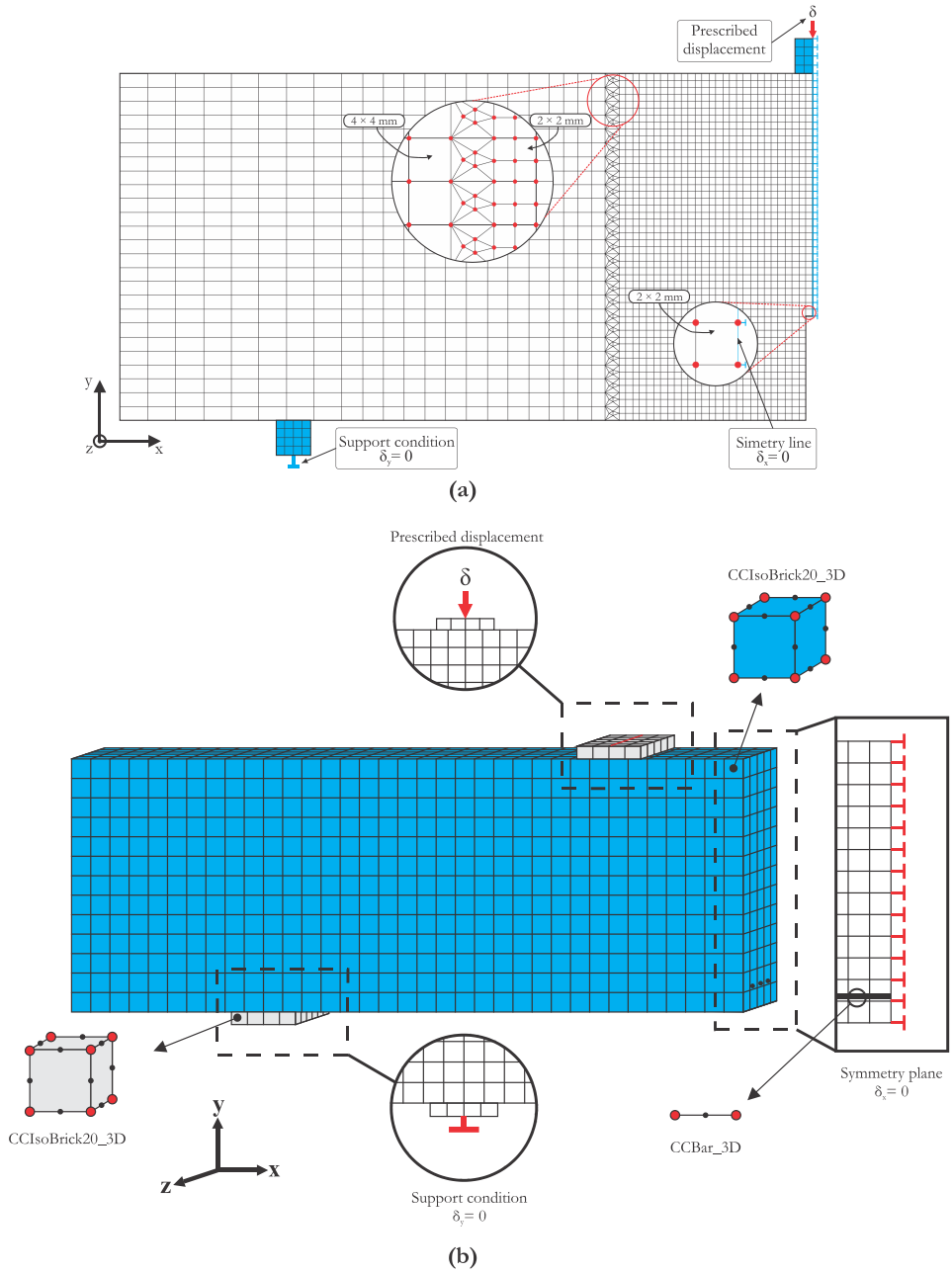

Figure 8. Finite element mesh and boundary conditions: (a) notched specimen and (b) beam.

3. Results and analysis

3.1. *Experimental observations*

3.1.1. NC-S and NC-L beams

Table 4 provides the summary results for the test beams; the NC-S beam was shown to fail under diagonal tension. Under a load of 80 kN, the first flexural cracks in the beam central region could be observed. When the load level of 120 kN was reached, shear-flexural cracks were observed outside the maximum flexural moment region. Subsequently, diagonal shear cracks appeared with significant length in each shear span at load of 151 kN. As the load increase, the diagonal shear crack

located in the left span progressively increasing the opening. After a load level of 260 kN was reached, the diagonal cracks propagated towards the loading plates. Lastly, the beam failed in shear at a maximum load of 340.95 kN. The maximum measured strain in the longitudinal reinforcement reached 3.22 mm/m, exceeding the strain at the limit of proportionality (2.30 mm/m).

Table 4. Summary of test results for the RC and SFRC beams.

Beam	ρ_w [%]	ε_s^L [mm/m]	ε_s^S [mm/m]	ε_c [mm/m]	P_{max} [kN]	Failure mode
NC-S	0.14	3.22	4.32	–	340.95	Shear (1)
NC-L	–	3.18	–	2.05	370.49	Shear (2)
SF-L-0.57	–	15.75	–	4.38	432.29	Flexural–Shear
SF-L-0.76	–	15.93	–	4.22	442.71	Flexure

[Note] ρ_w = shear reinforcement ratio, ε_s^L = longitudinal reinforcement strain, ε_s^S = transverse reinforcement strain, ε_c = concrete strain, P_{max}= maximum load, (1) diagonal tension, and (2) shear–compression.

Figure 9(a) shows the final crack pattern of the beam. On the other hand, the NC-L beam failed in shear-compression, similar behaviors to NC-S beam were observed in terms of first flexural and shear-flexural cracks load. However, the diagonal shear crack was initiated at a higher load (161.11 kN). This is attributed to the fact that the tensile strength of concrete in the NC-S beam was lower than that of the NC-L beam (19.3%). The diagonal shear crack of the NC-L beam had a shorter length and a tortuous trajectory compared to the NC-S beam (Figure 9(b)). As the load increased, the crack propagated towards the left loading plate. Finally, the beam failed with shear at a maximum load of 370.49 kN, due to abrupt crushing of concrete in the top compression zone near the left side of the loading plate. The strains measured in the reinforcement of both beams exceed the proportionality limit slightly.

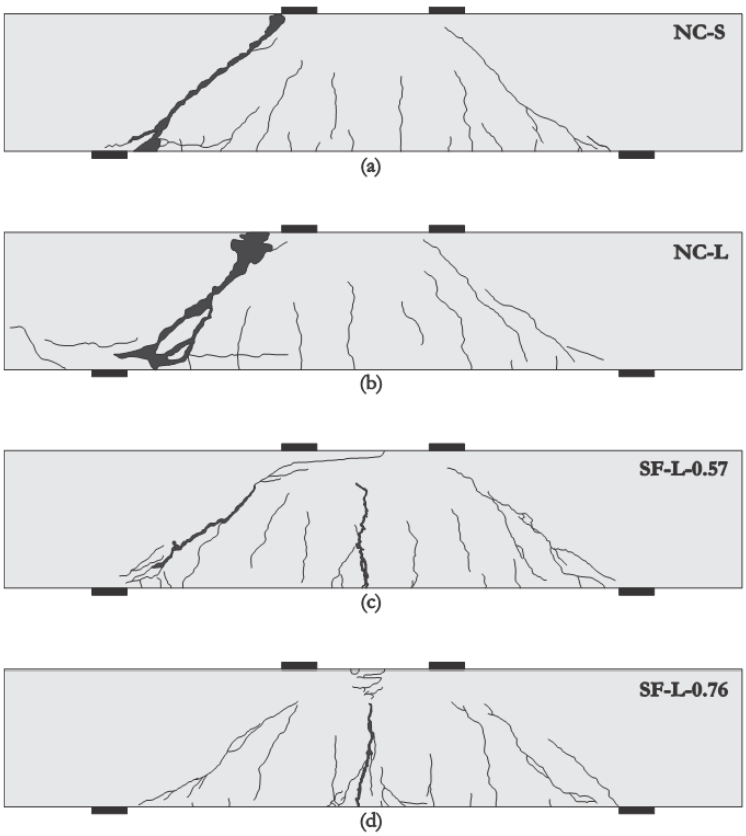

Figure 9. Crack patterns and failure modes: (a) diagonal tension, (b) shear-compression, (c) flexural–shear, and (d) flexure.

3.1.2. SF-L-0.57 and SF-L.0.76 beams

The SF-L-0.57 beam failed due to combined effects of flexural and shear stresses; the respective crack pattern of the beam is shown in Figure 9(c), which shows a vertical and diagonal crack with wide opening. The first flexural and shear-flexural cracks were formed with the same load level (120 kN). Compared with the beams without steel fibers this value is 50% higher. The diagonal shear crack was developed at 180 kN, its length was considerably shorter than that observed in the beams without steel fibers. As the load increased, the diagonal shear cracks propagated towards the loading plates without showing remarkable crack opening. When a load level of 422 kN was reached, the diagonal crack of the left shear span and the vertical crack in the mid-span increased gradually the opening. Finally, at 432.29 kN the beam failed due to the propagation of the shear diagonal crack describing a curved path to the central compression zone. The strain measured in the concrete compression zone exceeded the value of plastic strain, reaching a maximum strain of 4.38 mm/m. In addition, the strain in the longitudinal reinforcement significantly exceeded the yield strain of bars, reaching a strain of 15.75 mm/m. Regarding the SF-L-0.76 beam, it failed in flexure. The first flexural cracks were formed at 100 kN and similarly to the SF-L-0.57 beam the diagonal shear cracks were formed at 180 kN; nevertheless, these did not show visually significant openings as the load increased. After the longitudinal reinforcement initiated the yielding, the vertical crack located in the mid-span growth in the vertical direction, at the same time its opening increased. Finally, the beam failed in flexure due to crushing of concrete in the top compression zone.

3.2. *Numerical and experimental comparisons*

3.2.1. Load versus displacement curves of notched specimens

The numerical load versus displacement responses of the notched specimens are shown in Figure 10. These were obtained using the inverse analysis technique. A maximum number of four and seven iterations was required to obtain the calibrated curves of the SFRC-0.57 and SFRC-0.76, respectively. It is noteworthy that for the two types of concrete, the numerical curves are within the range of experimental results. The softening functions associated with these responses are presented in Figure 11.

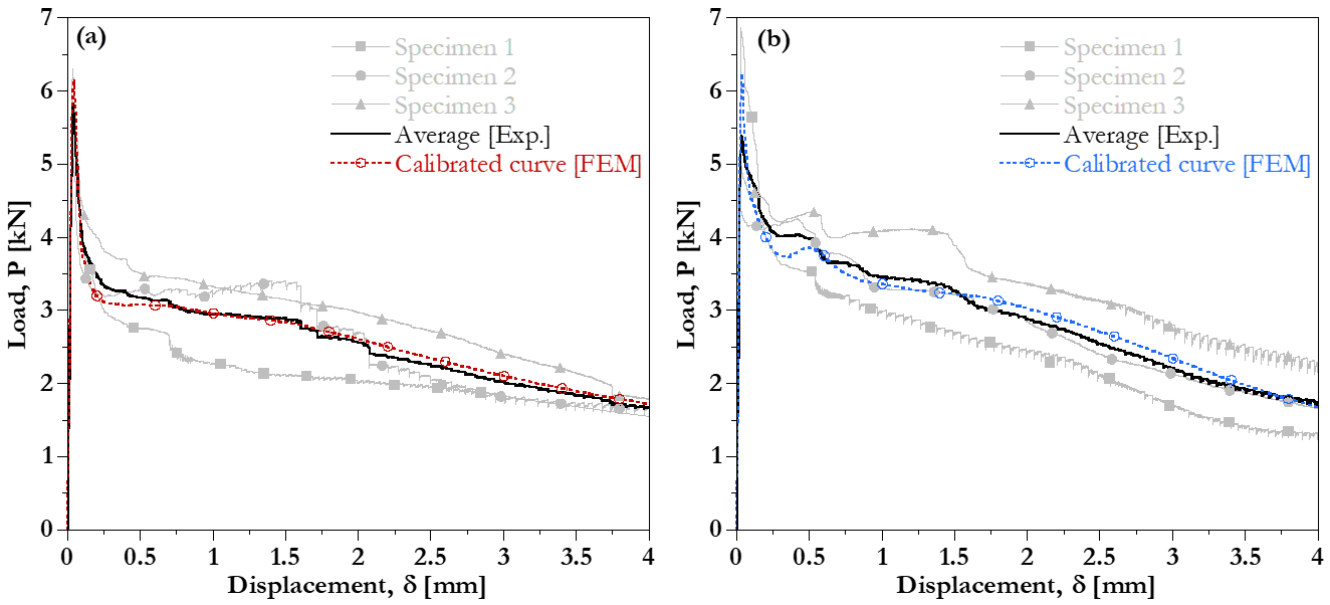

Figure 10. Calibrated curves of notched specimens obtained by inverse analysis: (a) SFRC–0.57 and (b) SFRC–0.76.

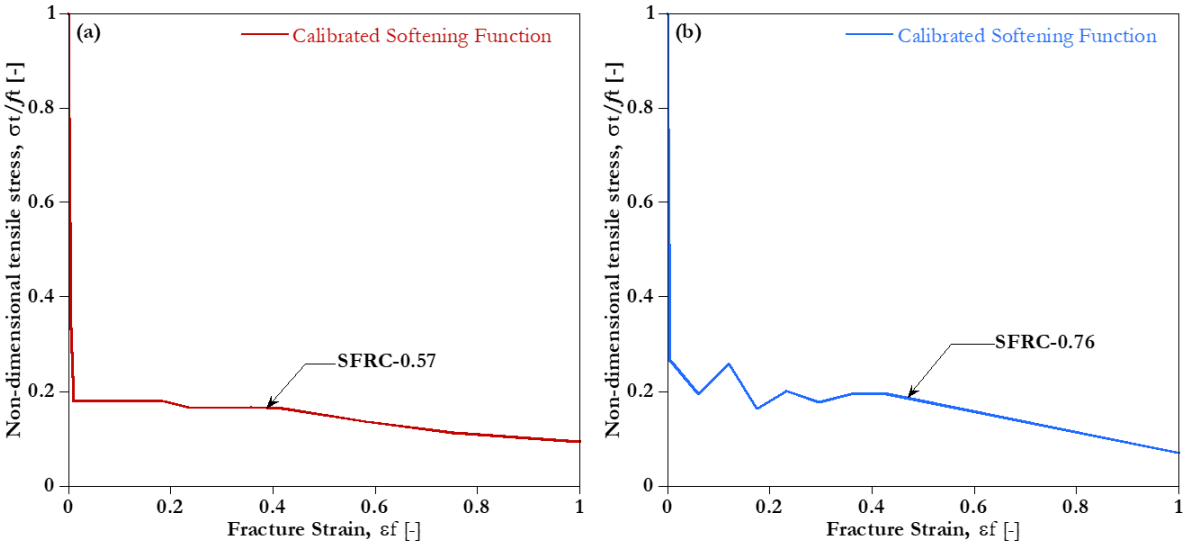

Figure 11. Calibrated softening functions: (a) SFRC–0.57 and (b) SFRC–0.76.

3.2.2. Load versus displacement curves of beams

Figure 12 compares the experimental and numerical load versus displacement curves of beams. The numerical results shown good agreement in terms of stiffness and maximum load. The responses of NC-S and NC-L beams are shown in Figure 12(a) and Figure 12(b), respectively. The numerical models were able to capture the behavior in terms of stiffnesses, it can be seen that this is greater in the NC-S beam, due to the contribution of the shear reinforcement. On the other hand, the failure load was predicted with relative error of 1.73% and 2.37%, for the NC-S and NC-L beam, respectively. Figure 12(c) shows the load versus displacement responses of SF-L-0.57 beam, it can be seen that the numerical stiffness has a similar tendency to that measured in the test. In addition, it was also possible to capture the plateau in the post peak regime, related with the yielding of the longitudinal reinforcement and the fibers bridging mechanism. The steel fibers controlled the unstable propagation of the shear diagonal cracks for a longer time, providing ductility. The maximum load was predicted with relative error of 2.73%. Finally, the load versus displacement curves of SF-L-0.76 are shown in Figure 12(d), the results shown good agreement, a relative error of 3.47% was reached in term of maximum load.

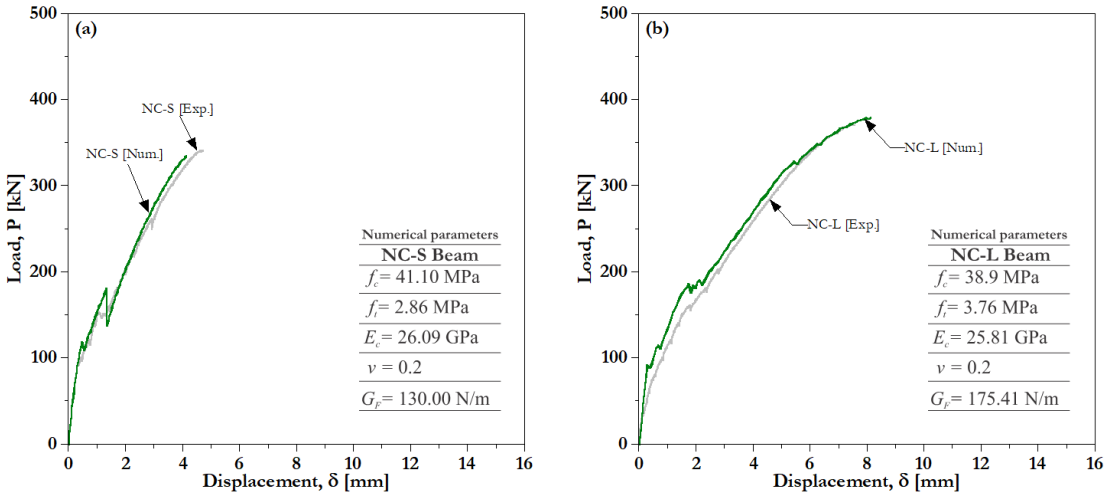

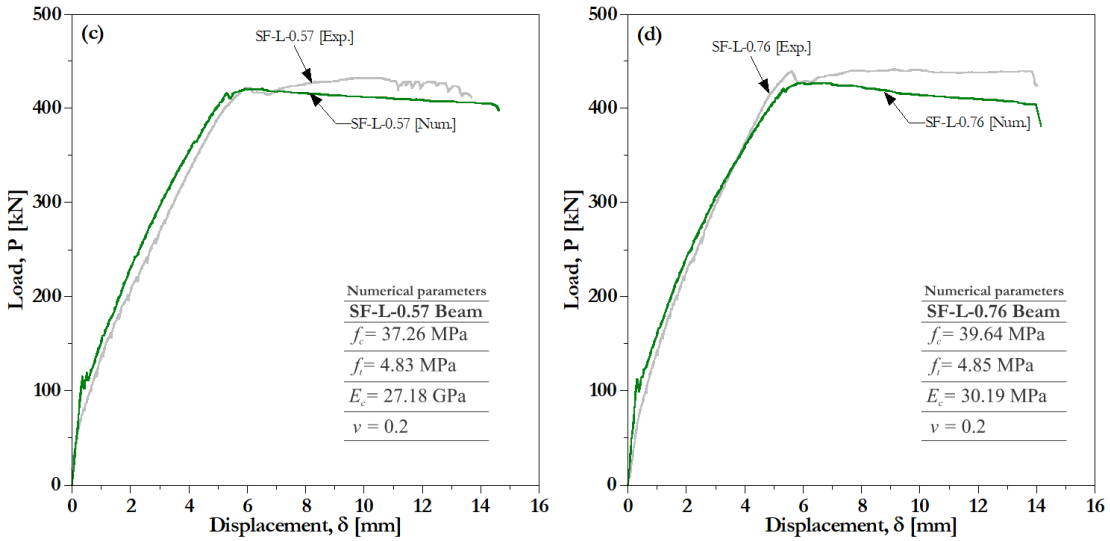

Figure 12. Experimental and numerical load versus displacement curves: (a) NC-S, (b) NC-L, (c) SF-L-0.57 and (d) SF-L-0.76.

Table 5 compares the first flexural crack load, shear diagonal crack load and shear failure. A good approximation can be observed between the experimental and numerical values of the failure shear. Figure 13 shows a comparison between experimental and predicted shear ultimate capacity.

Table 5. Comparison between experimental results and numerical predictions.

Beam	Experimental [kN]			Numerical [kN]			Exp. / Num.		
	$P_{F,crack}$	$V_{S,crack}$	$V_{Failure}$	$P_{F,crack}$	$V_{S,crack}$	$V_{Failure}$	$P_{F,crack}$	$V_{S,crack}$	$V_{Failure}$
NC-S	80	75.5	170.5	112.5	90.0	167.5	0.71	0.84	1.02
NC-L	80	80.5	185.2	91.9	93.6	189.6	0.87	0.86	0.98
SF-L-0.57	120	90.0	216.1	115.6	–	210.2	1.04	–	1.03
SF-L-0.76	100	90.0	221.3	112.0	–	213.6	0.89	–	1.04

[Note] $P_{F,crack}$ = first flexural crack, $V_{S,crack}$ = shear diagonal crack, and $V_{Failure}$ = shear capacity.

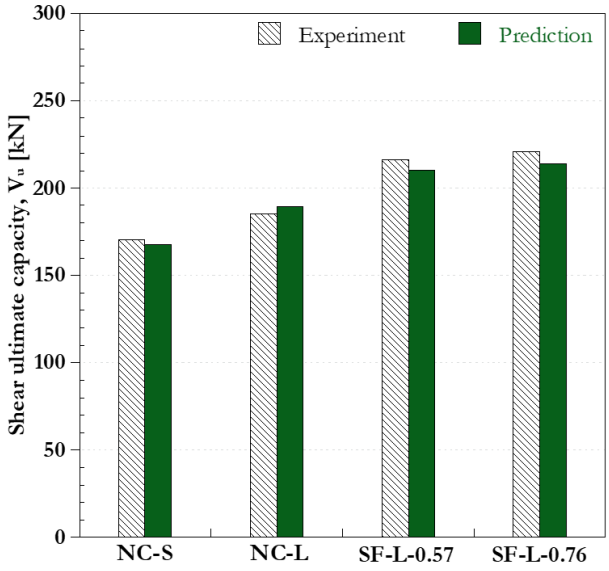

Figure 13. Experimental and numerical shear ultimate capacity.

3.2.3. Load versus steel strain curves of beams

In Figure 14(a) are shown the stress versus strain curves of longitudinal reinforcement of NC-S and NC-L beams. It is possible to verify that the yielding strain is slightly exceeded, which confirms the brittle failure of those beams. On the other hand, the SFRC beams developed ductile behavior, reaching higher strains that exceeded the yielding strain of reinforcement bars (Figure 14(b)). Regarding stirrup strains from the NC-S beam, in Figure 14(c) it can be seen that the strains have a null value until the growth of the shear diagonal crack. This behavior is associated to the fact that the tensile strains in the stirrup are concentrated in different positions as the load increases. Prior to the growth of the shear diagonal crack, the strains were not able to concentrate in the monitored point by the strain gage (SG1), so the strains were null until then.

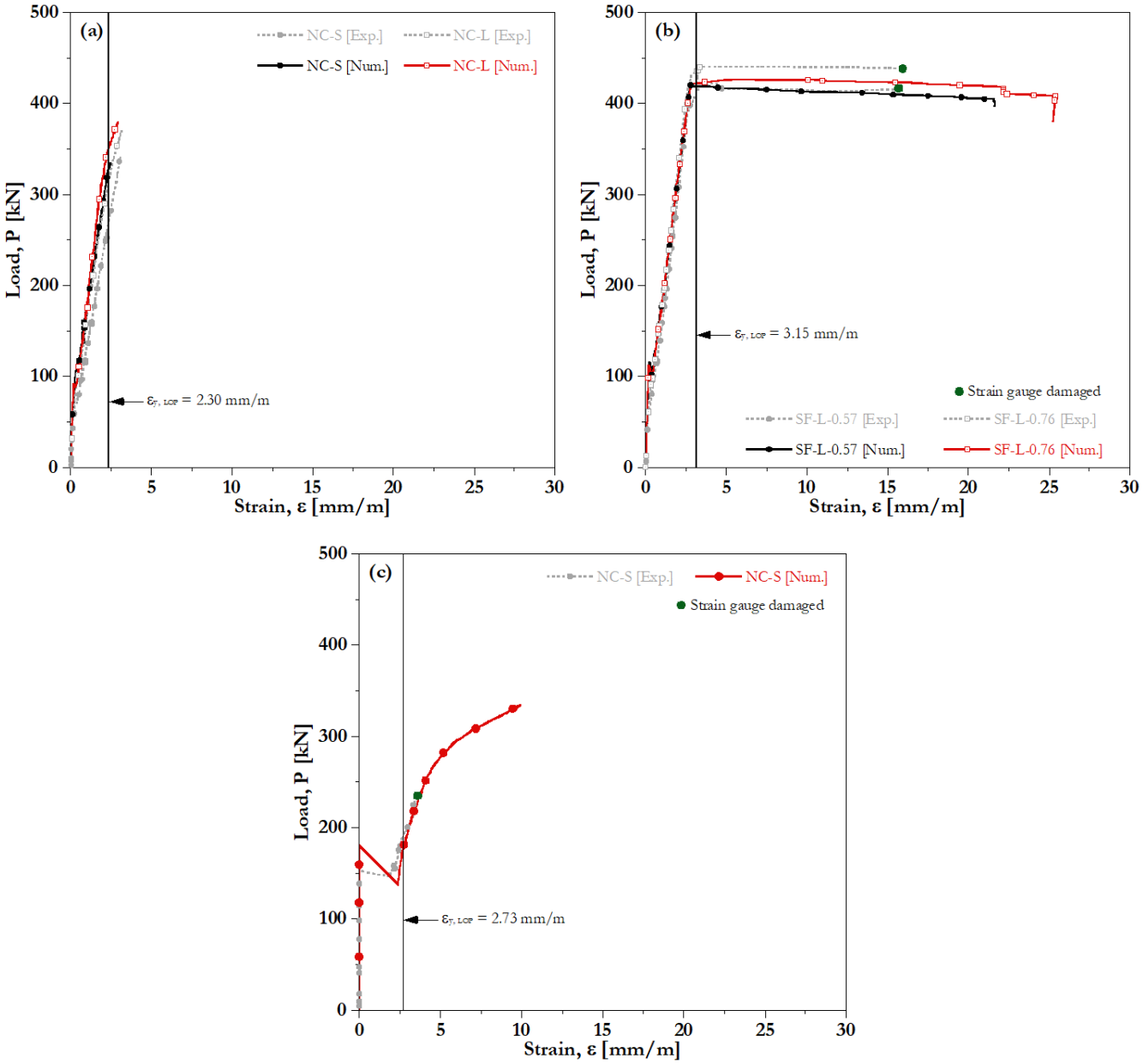

Figure 14. Experimental and numerical load versus strain relationships: (a) longitudinal reinforcement of NC-S and NC-L beams, (b) longitudinal reinforcement of SF-L-0.57 and SF-L-0.76 beams and (c) transverse reinforcement of NC-S beam.

3.2.4. Crack patterns and failure modes of beams

Pictures of the experimental crack patterns after failure, the localization of principal tensile strains, and distribution of principal compressive stress, are illustrated in Figure 15. The stress and strains states presented correspond to the step prior to failure in each model. The numerical crack patterns are represented by black lines together with the principal compressive stress; a filter was applied so that only cracks greater than 0.1 mm were shown. It can be seen that in the beams where only one significant opening crack was developed, for example, NC-S, NC-L and SF-L-0.76 beams, the models reproduced their location with good agreement. However, in the case of the SF-L-0.57 beam where two cracks (diagonal and flexural) developed significant openings, the model showed limitations for reproducing the location of one of them. For this beam it was only possible to represent the location of the flexural crack. The models developed in this study consider that the mechanical properties of the SFRC are homogeneously distributed in all the finite elements. In a real scenario, during the casting procedure of beams, there is the possibility of regions with poor fiber distribution. This phenomenon becomes more significant in situations where a low volume of fibers is added, as is the case of the SF-L-0.57 beam. Standards such as ACI318-19 (ACI, 2019) suggest that for structural applications steel fiber volumes greater than 0.75% should be used.

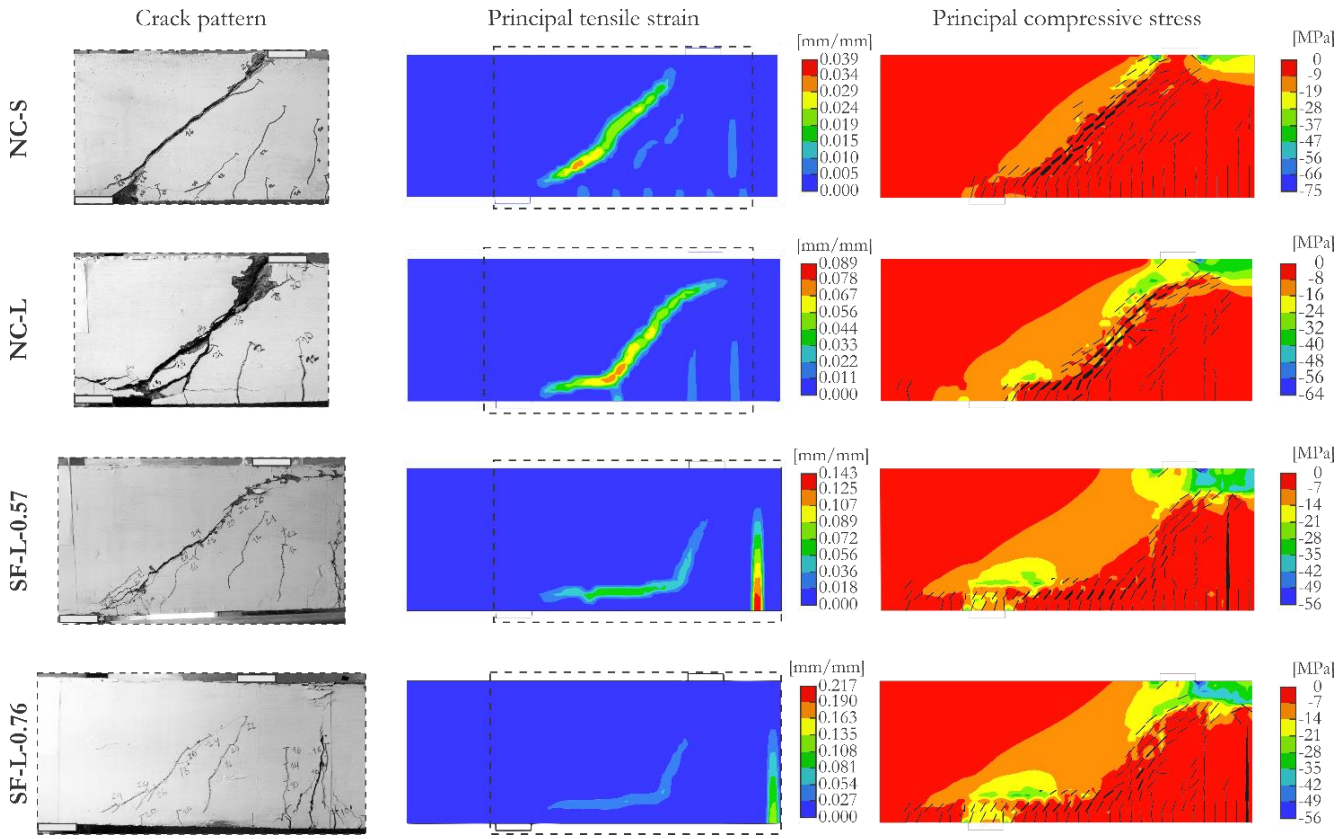

Figure 15. Experimental and numerical crack patterns, principal tensile strains and principal compressive stresses.

The numerical models were able to reproduce the cracking in localized regions of the beams. Figure 16(a) shows the crack pattern of SF-L-0.57 beam, in this case crack openings even smaller were filtered (0.01 mm). Horizontal cracks due to crushing of concrete can be visualized along with the region of high concentration of compressive stresses. On the other hand, Figure 16(b) showed the location of the principal tensile strains of the NC-L beam, it can be observed that these are distributed along the longitudinal reinforcement producing the horizontal splitting cracks.

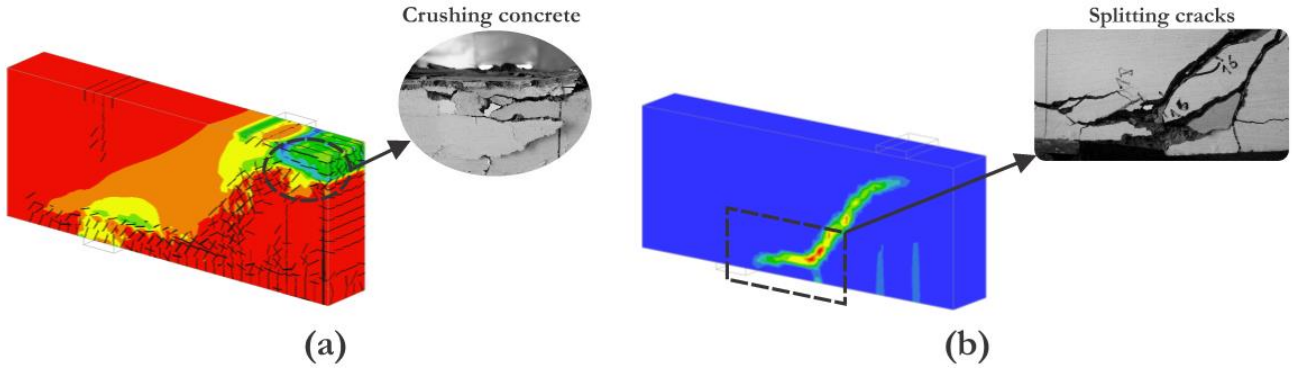

Figure 16. Localized fractures: (a) crushing concrete in SF-L-0.57 beam and (b) horizontal splitting cracks in NC-L beam.

4. Conclusions

In this paper, nonlinear finite element analysis and inverse analysis were used to predict the capacity and ultimate behavior of reinforced concrete and steel fiber reinforced concrete beams. The ATENA software, based on the smeared crack approach and crack band theory, was used for the modeling of notched specimens and beams. The conclusions of this study are summarized below:

1. Normal concrete fracture can be satisfactorily modeled using *CC3DnonLinCementitious* material model of ATENA. The numerical models of the beams with and without stirrups were able to predict the relationships load versus displacement, load versus strain, crack patterns and failure modes with good acceptance.
2. The post-cracking response of notched specimens was numerically reproduced with good acceptance, by means of the tensile softening functions calibrated by inverse analysis. Additionally, it was possible to predict the ultimate capacity of SFRC beams by applying these functions in the models.
3. Inverse analysis technique is a methodology with potential for the analysis of structural engineering problems where it is required to evaluate the ultimate behavior of SFRC beams. The indirect acquisition of post-cracking material response through the numerical three-point bending test calibration is shown as an advantageous and practical alternative in situations where it is not possible to execute the direct tensile test.
4. The assumption of homogeneous distribution of the mechanical properties of the SFRC in all the finite elements of the model may present some limitations for predicting the crack pattern of reinforced beams with low fiber volumes. In this case, the great heterogeneity in mechanical properties can lead to the propagation of cracks in beam regions subjected to complex stress states and poor fiber distribution.

Author contributions: Carlos A. Benedetty: Investigation, Data curation, Writing - original draft. Ingrid R. Irreño: Conceptualization, Methodology, Writing - original draft. Juan J. Martinez: Conceptualization, Methodology, Writing - original draft. Luiz C. Almeida: Writing - review & editing, Supervision, Project administration, Funding acquisition. Leandro M. Trautwein: Writing - review & editing, Supervsion, Project administration, Funding acquisition. Pablo A. Krahl: Writing - review & editing.

Funding: This study was supported by the Brazilian Coordination for the Improvement of Higher Education Personnel (CAPES) and Brazilian National Council for Scientific and Technological Development (CNPq).

Acknowledgments: The authors greatly appreciate the financial support provided by the Brazilian Coordination for the Improvement of Higher Education Personnel (CAPES) (Project No. 01-P-01879-2016), and the Brazilian National Council for Scientific and Technological Development (CNPq) (Project No. 140135/2019-7). They also thank the Structural Modeling and Monitoring Laboratory (LabMEM) for the support and the laboratory facilities to perform the tests.

Conflicts of interest: The authors declare that they have no known competing financial interests or personal relationships that could have appeared to influence the work reported in this paper.

References

ABNT-Brazilian National Technical Standards Association. (2007). NBR 5739: Concrete-Compression test of cylindric specimens-Method of test.

ABNT-Brazilian National Technical Standards Association. (2008). NBR 8522: Concrete-Determination of the elasticity modulus by compression.

ABNT-Brazilian National Technical Standards Association. (2011). NBR 7222: Concrete and mortar-Determination of the tension strength by diametrical compression of cylindrical test specimens.

ACI 318M-19. (2019). Building Code Requirements for Structural Concrete and Commentary, American Concrete Institute, ACI Committee 318, Farmington Hills, MI.

ASTM A-370. (2012). Standard Test Methods and Definitions for Mechanical Testing of Steel Products, American Society for Testing Materials, ASTM International, West Conshohocken, PA.

ASTM E8/E8M-16a. (2016). Standard Test Methods for Tension Testing of Metallic Materials, American Society for Testing Materials. ASTM International, West Conshohocken, PA.

Barros, J. A., & Figueiras, J. A. (1999). Flexural behavior of SFRC: testing and modeling. *Journal of materials in civil engineering*, *11*(4), 331-339.

Barros, J., Sanz, B., Kabele, P., Yu, R. C., Meschke, G., Planas, J., Cunha, V., Caggiano, A., Ozyurt, N., Gouveia, V., van den Bos, A., Poveda, E., Gal, E., Cervenka, J., Neu, G. E., Rossi, P., Dias-da-Costa, D., Juhasz, P. K., Cendon, D., … Valente, T. (2021). Blind competition on the numerical simulation of steel-fiber-reinforced concrete beams failing in shear. *Structural Concrete*, *22*(2), 939–967. https://doi.org/10.1002/suco.202000345.

Banthia, N., & Trottier, J. F. (1994). Concrete reinforced with deformed steel fibers, part I: bond-slip mechanisms. *Materials Journal*, 91(5), 435-446.

Bažant, Z. P., & Oh, B. H. (1983). Crack band theory for fracture of concrete. *Matériaux et construction*, 16(3), 155-177.

Benedetty, C.A. (2018). Experimental and numerical analysis of the behavior of reinforced concrete beams with steel fibers (M.Sc. Thesis, University of Campinas, Campinas, Brazil). [in Portuguese].

Cattaneo, S., & Rosati, G. (1999). Effect of different boundary conditions in direct tensile tests: experimental results. *Magazine of Concrete Research*, 51(5), 365-374.

Cugat, V., Cavalaro, S. H. P., Bairán, J. M., & de la Fuente, A. (2020). Safety format for the flexural design of tunnel fibre reinforced concrete precast segmental linings. *Tunnelling and Underground Space Technology*, *103*. https://doi.org/10.1016/j.tust.2020.103500.

Červenka, J., & Papanikolaou, V. K. (2008). Three dimensional combined fracture-plastic material model for concrete. *International Journal of Plasticity*, *24*(12), 2192–2220. https://doi.org/10.1016/j.ijplas.2008.01.004.

Červenka, V., Jendele, L., & Červenka, J. (2021). ATENA Program Documentation–Part 1. Cervenka Consulting sro.

de Montaignac, R., Massicotte, B., Charron, J. P., & Nour, A. (2012). Design of SFRC structural elements: Post-cracking tensile strength measurement. In *Materials and Structures/Materiaux et Constructions* (Vol. 45, Issue 4, pp. 609–622). https://doi.org/10.1617/s11527-011-9784-z.

de Oliveira e Sousa, J. L. A., & Gettu, R. (2006). Determining the Tensile Stress-Crack Opening Curve of Concrete by Inverse Analisis. *Journal Of Engineering Mechanics*, *132*(2), 141–148. https://doi.org/10.1061/(ASCE)0733-9399(2006)132:2(141).

de Souza, R. A., & Breña, S. F. (2020). Simplified nonlinear analysis of reinforced concrete coupling beams subjected to cyclic loading. Revista de La Construccion, 19(3), 224–232. https://doi.org/10.7764/RDLC.19.3.224.

Di Prisco, M., & Plizzari, G. (2004). Precast SFRC elements: From material properties to structural applications. In 6th RILEM symposium on fibre-reinforced concretes FRC-BEFIB 2004, Varenna, Italy, september 20-22, 2004 (pp. 81-100). RILEM Publication sarl.

Dupont, D., & Vandewalle, L. (2002). Recommendations for Testing of SFRC: Report of Subtask 7.1: Final Report. Test and Design Methods for Steel for Steel Fibre Reinforced Concrete, Brite Euram BRPR-CT98-0813 Project No: BE, 97-4163.

Sanabria Díaz, R. A., Sarmiento Nova, S. J., Teixeira da Silva, M. C. A., Mouta Trautwein, L., & de Almeida, L. C. (2020). Reliability analysis of shear strength of reinforced concrete deep beams using NLFEA. *Engineering Structures*, *203*. https://doi.org/10.1016/j.engstruct.2019.

FIB. (2010). fib Model Code 2010. Federation Internationale du Beton, Bulletin 65/66, Lausanne, Switzerland.

Gali, S., & Subramaniam, K. V. L. (2018). Multi-linear stress-crack separation relationship for steel fiber reinforced concrete: Analytical framework and experimental evaluation. *Theoretical and Applied Fracture Mechanics*, *93*, 33–43. https://doi.org/10.1016/j.tafmec.2017.06.

GID. (2009). The Personal Pre and Post Processor. International Center for Numerical Methods in Engineering Barcelona.

Gribniak, V., Kaklauskas, G., Hung Kwan, A. K., Bacinskas, D., & Ulbinas, D. (2012). Deriving stress-strain relationships for steel fibre concrete in tension from tests of beams with ordinary reinforcement. *Engineering Structures*, *42*, 387–395. https://doi.org/10.1016/j.engstruct.2012.04.

Hordijk, D.A. (1991). Local approach to fatigue of concrete (PhD Thesis, Delft University of Technology, Delft, Netherlands).

JCI. (2003). Method of test for fracture energy of concrete by use of notched beam. JCI-S-001e2003, Japan Concrete Institute Standard, Tokyo, Japan.

JCI. (2003). Method of test for load-displacement curve of fiber reinforced concrete by use of notched beam. JCI-S-002-2003, Japan Concrete Institute Standard, Tokyo, Japan.

Kannam, P., & Sarella, V. R. (2018). A study on validation of shear behaviour of steel fibrous SCC based on numerical modelling (ATENA). *Journal of Building Engineering*, *19*, 69–79. https://doi.org/10.1016/j.jobe.2018.05.

Kasuga, A. (2017). Effects of butter web design on bridge construction. *Structural Concrete*, *18*(1), 128–142. https://doi.org/10.1002/suco.

Lee, J. H., Cho, B., & Choi, E. (2017). Flexural capacity of fiber reinforced concrete with a consideration of concrete strength and fiber content. *Construction and Building Materials*, *138*, 222–231. https://doi.org/10.1016/j.conbuildmat.2017.01.

Li, B., Xu, L., Chi, Y., Huang, B., & Li, C. (2017). Experimental investigation on the stress-strain behavior of steel fiber reinforced concrete subjected to uniaxial cyclic compression. *Construction and Building Materials*, *140*, 109–118. https://doi.org/10.1016/j.conbuildmat.2017.02.

Li, B., Xu, L., Shi, Y., Chi, Y., Liu, Q., & Li, C. (2018). Effects of fiber type, volume fraction and aspect ratio on the flexural and acoustic emission behaviors of steel fiber reinforced concrete. *Construction and Building Materials*, *181*, 474–486. https://doi.org/10.1016/j.conbuildmat.2018.06.

Menetrey, P., & Willam, K. J. (1995). Triaxial failure criterion for concrete and its generalization. *Structural Journal*, *92*(3), 311-318.

Nour, A., Massicotte, B., de Montaignac, R., & Charron, J. P. (2015). Development of an inverse analysis procedure for the characterisation of softening diagrams for FRC beams and panels. *Construction and Building Materials*, *94*, 35–44. https://doi.org/10.1016/j.conbuildmat.2015.06.049.

Planas, J., Guinea, G. V., & Elices, M. (1999). Size effect and inverse analysis in concrete fracture. *International Journal of Fracture*, *95*(1), 367-378.

Poveda, E., Yu, R. C., Tarifa, M., Ruiz, G., Cunha, V. M. C. F., & Barros, J. A. O. (2020). Rate effect in inclined fibre pull-out for smooth and hooked-end fibres: a numerical study. *International Journal of Fracture*, *223*(1–2), 135–149. https://doi.org/10.1007/s10704-019-00404-7.

Sajdlová, T. (2016). ATENA Program Documentation. Part 4-7. ATENA Science – GiD FRC Tutorial. Červenka Consulting, Prague.

Serna, P., Arango, S., Ribeiro, T., Núñez, A. M., & Garcia-Taengua, E. (2009). Structural cast-in-place SFRC: Technology, control criteria and recent applications in spain. *Materials and Structures/Materiaux et Constructions*, *42*(9), 1233–1246. https://doi.org/10.1617/s11527-009-9540-9.

Sheng, P., Zhang, J., & Ji, Z. (2016). An advanced 3D modeling method for concrete-like particle-reinforced composites with high volume fraction of randomly distributed particles. *Composites Science and Technology*, *134*, 26–35. https://doi.org/10.1016/j.compscitech.2016.08.009.

Soltanzadeh, F., Cunha, V. M. C. F., & Barros, J. A. O. (2019). Assessment of different methods for characterization and simulation of post-cracking behavior of self-compacting steel fiber reinforced concrete. *Construction and Building Materials*, *227*. https://doi.org/10.1016/j.conbuildmat.2019.116704.

Uchida, Y., Kurihara, N., Rokugo, K., & Koyanagi, W. (1995). Determination of tension softening diagrams of various kinds of concrete by means of numerical analysis. *Fracture mechanics of concrete structures*, *1*, 17-30.

van Mier, J. G. (1986). Multiaxial strain-softening of concrete. *Materials and structures*, *19*(3), 190-200.

Wang, Z. L., Wu, J., & Wang, J. G. (2010). Experimental and numerical analysis on effect of fibre aspect ratio on mechanical properties of SRFC. *Construction and Building Materials*, *24*(4), 559–565. https://doi.org/10.1016/j.conbuildmat.2009.09.009.

Woo, S. K., Kim, K. J., & Han, S. H. (2014). Tensile cracking constitutive model of Steel Fiber Reinforced Concrete (SFRC). *KSCE Journal of Civil Engineering*, *18*(5), 1446–1454. https://doi.org/10.1007/s12205-014-0335-3.

Yoo, D. Y., Yoon, Y. S., & Banthia, N. (2015). Predicting the post-cracking behavior of normal- and high-strength steel-fiber-reinforced concrete beams. *Construction and Building Materials*, *93*, 477–485. https://doi.org/10.1016/j.conbuildmat.2015.06.006.

Zhang, H., Huang, Y. J., Yang, Z. J., Xu, S. L., & Chen, X. W. (2018). A discrete-continuum coupled finite element modelling approach for fibre reinforced concrete. *Cement and Concrete Research*, *106*, 130–143. https://doi.org/10.1016/j.cemconres.2018.01.010.

Zhang, S., Zhang, C., Liao, L., Wang, C., & Zhao, R. (2020). Investigation into the effect of fibre distribution on the post-cracking tensile strength of SFRC through physical experimentation and numerical simulation. *Construction and Building Materials*, *248*. https://doi.org/10.1016/j.conbuildmat.2020.118433.